nature astronomy

Article

https://doi.org/10.1038/s41550-025-02640-5

KREEP-like lithologies in the South Pole–Aitken basin reworked by the Apollo basin impact at 4.16 Ga

Received: 21 January 2025

Accepted: 28 July 2025

Jingyou Chen [1,2,9], **Le Zhang** [1,2,9], **Zexian Cui** [1,2], **Zhiming Chen** [1,2,3], **Zhiyong Xiao** [4], **Fanglu Luo** [4], **Yuqi Qian** [5], **Yan-Qiang Zhang** [1,2], **Chengyuan Wang** [1,2], **Jintuan Wang** [1,2], **Qing Yang** [1,2], **Pengli He** [1,2], **Linli Chen** [1,2], **Fangfang Huang** [1,2], **Haiyang Xian** [1,2], **Katherine H. Joy** [6], **James W. Head** [7], **Clive R. Neal** [8] & **Yi-Gang Xu** [1,2] ✉

The early impact flux recorded by the Moon, especially the first billion years during the basin-forming epoch, is pivotal to understanding the evolution of inner Solar System bodies. However, our current understanding of this critical epoch is impeded by the lack of samples that have a clear provenance from specific ancient impact basins. Here we examine three impact-melt clasts in the Chang'e-6 lunar regolith collected from the Apollo basin within the gigantic South Pole–Aitken basin. We found that the impact-melt rocks, which have KREEP-like compositional signatures, probably originated from the differentiates of a South Pole–Aitken basin impact-melt sheet or pool, which were later reworked by the Apollo basin-forming event at ~4.16 Ga. This study suggests that the basin-forming epoch did not occur within the narrow timespan of ~3.8–4.0 Ga proposed for a cataclysmic late heavy bombardment.

The KREEP (potassium, rare-earth elements, phosphorus and other incompatible elements) geochemical signature is found in different rock types across the Moon[1], including igneous rocks (that is, >3.8 Ga lithologies such as extrusive KREEP basalts and ancient intrusive Mg- and alkali-suites) as well as in impact-melt or melt breccias[2]. KREEP is believed to be a key component of the late-stage products of lunar magma ocean crystallization (that is, urKREEP)[3]. Global surface mapping of the incompatible element Th has shown an asymmetrical KREEP distribution pattern, with higher abundances on the nearside Procellarum KREEP Terrane and low concentrations on the farside Feldspathic Highland Terrane[4]. The general deficiency of farside KREEP has been attributed to displacement of these materials in the mantle towards the nearside by the South Pole–Aitken (SPA) impact[5]. Nevertheless, some KREEP-rich areas have still been detected within the lunar farside SPA basin[6] and in some unique farside places, such as Compton-Belkovich[7]. Several proposed scenarios[6,8] for interpreting the origin of KREEP materials within the SPA region remain controversial, and understanding the rock carriers of KREEP remotely observed in the SPA basin requires direct study of samples returned from this region.

Following the Moon's giant-impact origin, large impacts were the dominant geological processes shaping the Moon after solidification of an hypothesized magma ocean[9]. Termed late heavy bombardment

---

[1] State Key Laboratory of Deep Earth Processes and Resources, Guangzhou Institute of Geochemistry, Chinese Academy of Sciences, Guangzhou, China. [2] Center for Advanced Planetary Sciences, Guangzhou Institute of Geochemistry, Chinese Academy of Sciences, Guangzhou, China. [3] College of Earth and Planetary Sciences, University of Chinese Academy of Sciences, Beijing, China. [4] Planetary Environmental and Astrobiological Research Laboratory, School of Atmospheric Sciences, Sun Yat-sen University, Zhuhai, China. [5] Department of Earth Sciences, GIGCAS-HKU Joint Laboratory of Chemical Geodynamics, The University of Hong Kong, Hong Kong, China. [6] Department of Earth and Environmental Sciences, The University of Manchester, Manchester, UK. [7] Department of Earth, Environmental and Planetary Sciences, Brown University, Providence, RI, USA. [8] Department of Civil and Environmental Engineering and Earth Sciences, University of Notre Dame, Notre Dame, IN, USA. [9] These authors contributed equally: Jingyou Chen, Le Zhang. ✉e-mail: yigangxu@gig.ac.cn

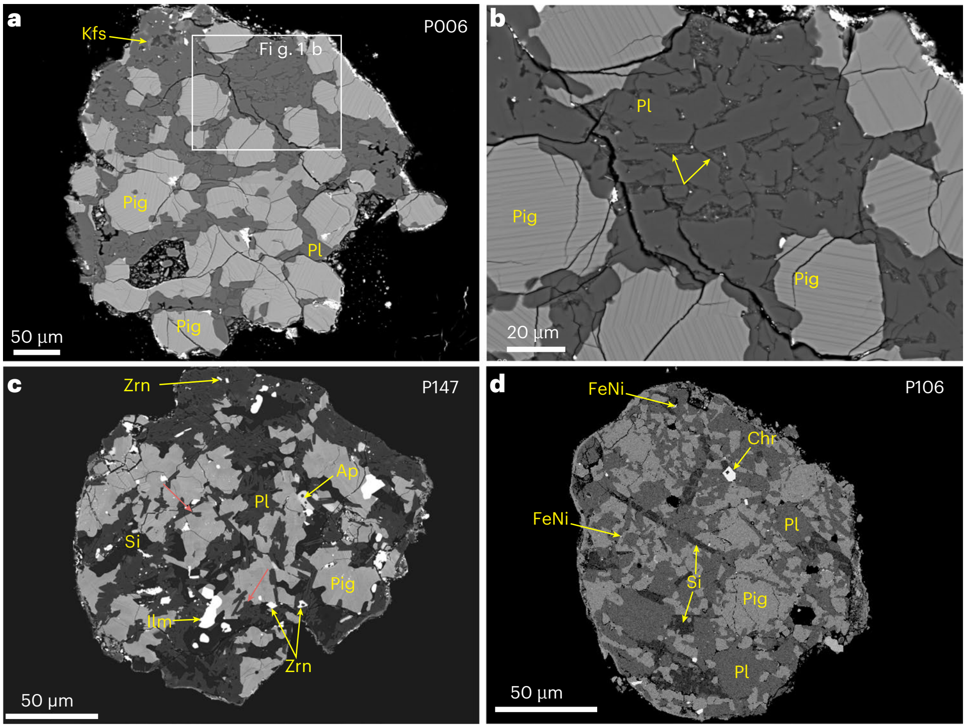

Fig. 1 | Backscattered electron (BSE) images of three impact-melt fragments. **a**, Porphyritic pigeonites immersed into fine-grained plagioclase grains (P006). **b**, A close view of image A showing exsolution lamellae within pigeonites and Si–K-rich intercumulus melt (yellow arrows). **c**, Irregular pigeonites (containing exsolution lamellae) dispersed within the plagioclase–silica matrix, and silica–plagioclase intergrowths showing a granophyric texture (P147). Small apatite, ilmenite and zircon grains are generally associated with plagioclase and Si–K intergrowths. The red arrows point to the penetration of plagioclase into adjacent pyroxene. **d**, A poikilitic–granoblastic texture for P106, which contains lathy and irregular amorphous silicas and FeNi metal grains. Pl, plagioclase; Kfs, K-feldspar; Pig, pigeonite; Ilm, ilmenite; Ap, apatite; Chr, chromite; Zrn, zircon; Si, silica; FeNi, FeNi alloy.

(LHB)[10], the impact flux of the basin-forming era remains a core debate in lunar and planetary science, and two-end member scenarios include (1) a gradually declining flux and (2) a flux peak at a narrow window of ~3.8–4.0 Ga or shorter[11]. The long and unresolved debate stems from the fact that most lunar impact basins lack precise sample-constrained radiometric formation ages[11]. Nevertheless, there is a consensus that precise formation ages of the Nectaris, Imbrium and Orientale basins would be the diagnostic information to resolve the impact flux during the LHB[12]. For these three basins, the Nectaris basin is critical as its age potentially marks the onset of the putative LHB[11]. While the Imbrium basin has a relatively well-defined age of ~3.92–3.94 Ga based on sample analyses[13] and the Orientale basin may have been formed at ~3.81 Ga (ref. 14), deciphered formation ages of the Nectaris basin from samples exhibit considerable uncertainties, that is, ~3.92 (ref. 15) to 4.26 Ga (ref. 16). Meanwhile, crater statistics and stratigraphic relationships of major lunar impact basins suggest that the farside Apollo basin was slightly younger than the nearside Nectaris[17], which is supported by their retention ages derived from crater statistics, that is, about 4.14 Ga and 4.1 Ga, respectively[14]. Therefore, as a close approximation for the formation age of the Nectaris basin, a precise sample-derived control for the formation age of the Apollo basin would provide an invaluable reference for the impact flux of the Moon during the LHB epoch[18].

The origin of KREEP-rich components in the SPA basin and the question of the Moon's LHB are addressed here by studying regolith samples returned by the Chang'e-6 (CE-6) mission, which landed in the southern interior of the Apollo basin, within the northeast region of the SPA basin[19]. CE-6 returned samples contain abundant exotic, non-mare materials (for example, anorthosite, norite, gabbro and impact-melt breccia) in addition to local mare basalts dated to be ~2.83 Ga (refs. 20,21), thereby providing an optimal opportunity to study lunar farside evolution. In this study, we focus on three impact-melt fragments (hereafter P006, P106 and P147) identified in the allocated CE-6 samples. We present the sample constraint on the age of the Apollo impact basin, and direct evidence for the presence of KREEP-like rocks on the lunar farside.

Impact-melt fragments

The three CE-6 non-mare fragments (150–350 µm) studied predominantly contain low-Ca pigeonite and plagioclase, with variable amounts of K-feldspar, silica (amorphous), Fe–Ni metal, zircon and apatite (Fig. 1). In terms of mineralogy, these fragments are compositionally similar to Apollo gabbros (fragments P006 and P106) and Apollo quartz monzodiorite (QMD) (fragment P147) (Fig. 2), although the two CE-6 gabbro fragments analysed here have mafic minerals that are more Fe-rich than Apollo Mg-suite gabbros (Fig. 2b). The grain size of the crystals in these fragments is typically <100 µm, indicating that they are more likely to be crystalline impact melts rather than endogenous intrusive bodies. The detailed description of their petrography and texture can be found in the Supplementary Text. Here, we outline the diagnostic characteristics of these lithic fragments that support our interpretation of their impact-derived origin.

First, FeNi particles in P106 exhibit Ni/Co ratios (11.2–14.6) consistent with the composition of exogenous metal found in a series of Apollo 16 impact-melt breccias (Extended Data Fig. 1), suggesting that this fragment has an impact-melt origin.

Second, the bimodal sizes between plagioclase (10–60 µm) and pyroxene (50–70 µm) in P006 reflect their mismatched cooling history, where the plagioclase cools much faster (~10^3 °C yr^{-1} estimated from the largest size of 60 µm (ref. 22)) than pigeonite (0.2–2.2 °C yr^{-1} calculated from 1–3 µm exsolved lamellae[23]). This contrasting cooling rate between plagioclase and pigeonite in the same sample is suggestive of the pyroxenes being xenocrysts in a secondary melt[24].

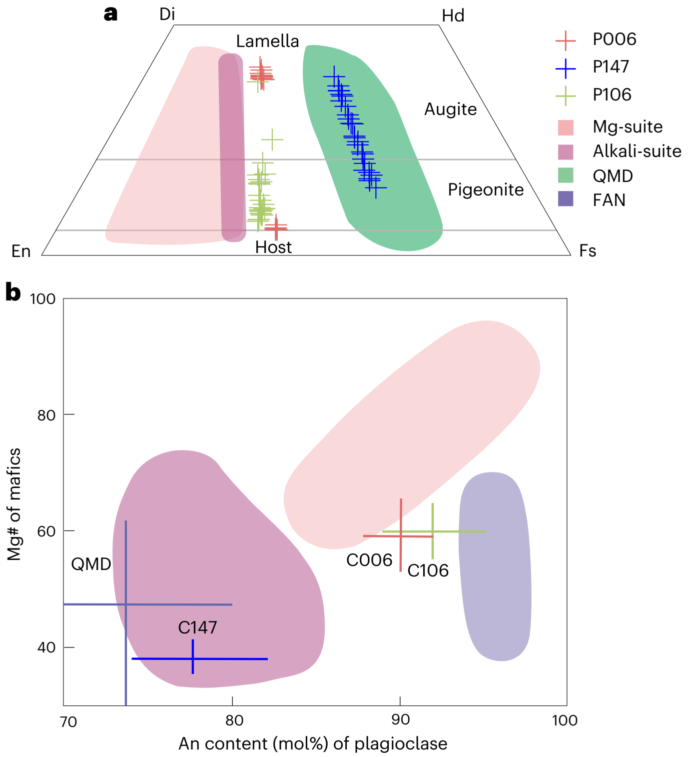

Fig. 2 | Composition plots of pyroxene and plagioclase in three CE-6 lithic fragments. **a**, A quadrilateral plot showing compositions of pyroxenes in three CE-6 lithic fragments, in comparison with Apollo QMD, alkali gabbro[64], and Mg-suite. **b**, A plot of An (plagioclase) versus Mg# (pyroxene). The line length of each sample reflects compositional ranges in three lithic fragments (P006: An_{88-92}, Mg# of 55–65; P106: An_{89-95}, Mg# of 58–61; P147: An_{72-81}, Mg# of 38–40) and Apollo QMD[65]. Compositional ranges of pristine non-mare Apollo Mg-suite, alkali-suite and ferroan anorthite (FAN) are from ref. 66.

Third, some of the margins of larger pigeonites adjacent to plagioclase have higher crystal orientations (Extended Data Fig. 2); high crystal orientations may be related to shock deformation, as any shock effect would be prominent at the two-phase interface, particularly when involving low-density plagioclase. Some lath-like Si-rich areas (50 µm) are glass and the exsolved pyroxenes have narrow widths of ~1 µm (Fig. 1d), suggesting a cooling rate near the threshold required for exsolution to occur.

Finally, some plagioclases in P147 penetrate into the adjacent pyroxene, akin to textures seen in Apollo KREEP basalt containing xenocrysts[25]. This fragment is compositionally similar to Apollo 15 QMD (Fig. 2), but has smaller crystal grain sizes than its counterpart Apollo 15 QMD[26], suggesting that it could cool rapidly from a parent melt of a QMD-like rock.

KREEP-bearing impact melts

The impact-melt fragments carry a strong KREEP signature, which is reflected by their trace element and Sr isotopic compositions. Specifically, pyroxenes in P147 and P006 have high rare-earth element (REE) abundance (Fig. 3a), comparable to and exceeding those in Apollo KREEP basalt, QMD and Mg-suite samples (Extended Data Fig. 3). The calculated REE compositions of melts in equilibrium with pigeonite and plagioclase from P147 and P006 are ~200–2,500 ×CI (Fig. 3c), comparable to Apollo KREEP basalts[27]. The Eu/Sm plot of plagioclase in P006 suggests a compositional similarity to Apollo KREEP basalts (Extended Data Fig. 4). The intercumulus melts (silica–K intergrowths) in P006 exhibit high-field-strength-element abundances similar to those of Apollo KREEP basalts (Fig. 3b), despite having conspicuously lower contents of other incompatible trace elements (ITEs), which probably resulted from the removal of phosphate phases within KREEP melts. Fragments P006, P147 and P106 have initial $^{87}\mathrm{Sr}/^{86}\mathrm{Sr}$ values of 0.69969 ± 0.00010 (2 s.d.), 0.69991 ± 0.00022 and 0.69995 ± 0.00020 (Fig. 3d), respectively, calculated to 4.16 Ga (see below), which concur well with the Sr isotopic evolution trajectory of the urKREEP source region ($^{87}\mathrm{Rb}/^{86}\mathrm{Sr}$ ratio of 0.215; Fig. 3d), similar to KREEP-rich Apollo impact-melt rocks[28]. Thus, the Sr isotope compositions of the three CE-6 impact-melt fragments suggest that they originate from KREEP-like precursors.

Origin of the KREEP-rich lithologies

Orbital measurements have revealed the presence of KREEP-rich materials within the interior of the SPA basin, with heterogeneous KREEP-like materials surrounding the SPA centre[29], near the CE-6 sampling site, which is located in the northeast of SPA interior (Extended Data Fig. 5). This suggests that there must be rocks containing a KREEP-like signature within the SPA basin. Several scenarios can be constructed to explain the origin of these materials: antipodal Imbrium impact ejecta from the Procellarum KREEP Terrane region[30], deep LMO residues (urKREEP) excavated by the SPA impact itself[31], and differentiates of the SPA impact-melt sheet or pool[8,32]. The first scenario can be discounted due to the fact that the Pb–Pb age (4.16 Ga, see next section) of the impact melts studied here predates the Imbrium basin age of approximately 3.9 Ga (ref. 13). However, the occurrence of KREEP-rich lithologies that were distributed by SPA impact proximal ejecta or within an SPA melt pool is supported by continuous Th-bearing materials around the SPA centre[29], with portions of the interior impact-melt region obscured by later cryptomare and mare deposits[33].

Recent work on the lunar meteorite Northwest Africa 2995[34] suggests that quartz monzogabbro lithologies within this sample could be representative of SPA KREEP-like impact melts. Accordingly, the precursor of the CE-6 KREEP-rich impact melt (P147) may originate from similar KREEP-rich SPA ejecta or KREEP-rich differentiates of an impact-melt sheet (Fig. 5a). Models indicate that the SPA-forming impact had penetrated to a depth of more than 50–100 km (ref. 35) to expose deeply buried KREEP materials, which were melted and mixed into an impact-melt pool or sheet on the floor of the basin. Given the low melting temperature of a subcrustal layer of urKREEP[36], the SPA impact-melt sheet would have potentially scavenged almost all KREEP components from the targeted area, leaving behind a very depleted mafic mantle source. This is consistent with a KREEP-free source of much later CE-6 sampled 2.83 Ga low-Ti mare basalts[20]. The differentiation of the SPA impact-melt sheet could have generated a cumulate pile made of ultramafic pyroxenite and dunite in the lower part and a norite layer in the upper part, consistent with spectroscopic and geophysical observations as well as thermal modelling[8,32]. Like the LMO case, the last ~0.5% of the impact-melt sheet would be KREEP-like in composition, as represented by the CE-6 impact-melt clasts reported here.

Constraints on the formation age of the Apollo basin

Pb–Pb isotope dating on Zr-bearing mineral, K-rich phase, apatite and pyroxene in the impact-melt fragments (Figs. 1 and 4) yield a weighted average Pb–Pb age of 4,165 ± 14 Ma (standard deviation, 2σ), despite the fact that two impact-melt fragments (P006 and P147) are from quite distinct lithological precursors (that is, a Mg-rich gabbro versus an Fe-rich QMD). Specifically, P106 yielded a Pb–Pb isochron age of 4,164 ± 7 Ma (2σ, probability of 0.31). A less robust age of 4,184 ± 40 Ma (2σ) is obtained for P147, given its probability of 0.006 (Fig. 4b). Nevertheless, this apparent age is identical within error to the isochron dating of P147 (Fig. 4b). The consistent ages of ~4.16 Ga obtained from the two impact-melt fragments probably reflect one (large) impact event, either the SPA basin impact or the Apollo basin impact. This interpretation is based on the source of the CE-6 KREEP-rich impact-melt samples, which

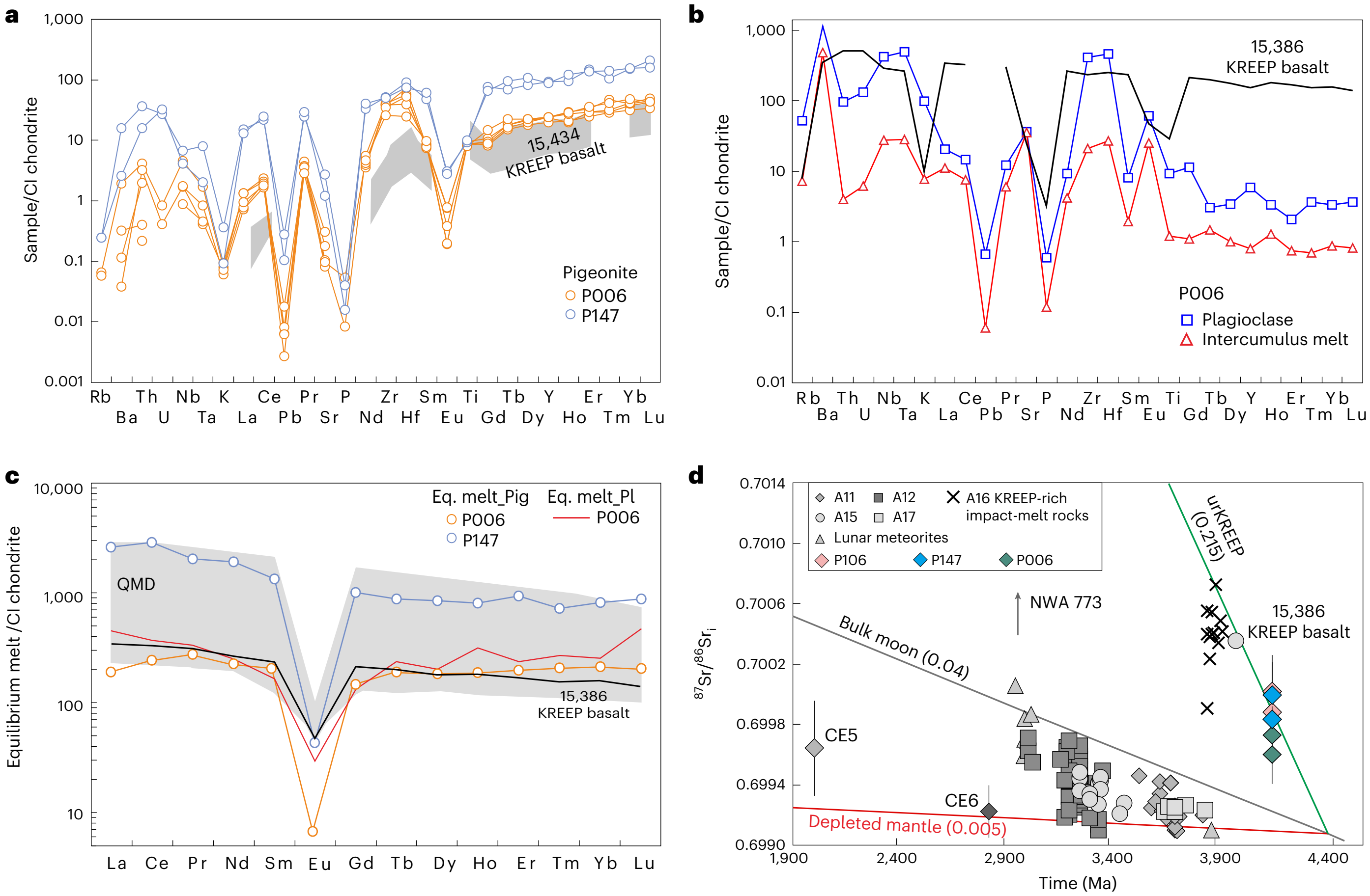

Fig. 3 | Trace elements of three CE-6 lithic fragments. a,**b**, Trace element diagrams of pigeonite (**a**) and plagioclase and intercumulus melt (**b**) from P006 and P147; the discontinuous fine grey lines represent the pigeonite REE in Apollo 15434 KREEP basalt[25]. **c**, Calculated REE concentrations of melts in equilibrium with plagioclase (Eq. melt_Pl) and pigeonite (Eq. melt_Pig) (Methods). Also shown for comparison are the REE patterns of intercumulus melt, Apollo 15386 KREEP basalt[27] and QMD[67]. **d**, Initial $^{87}Rb/^{86}Sr$ versus crystallization ages of lunar mare basalts and impact-melt rocks. The numbers in brackets are $^{87}Rb/^{86}Sr$ ratios of the sources. $^{87}Rb/^{86}Sr$ of other lunar mantle sources are fitted to these plotted lunar samples. The error bars are 2σ. The data for KREEP-rich Apollo impact-melt rocks are from ref. 28 and other data are from ref. 20.

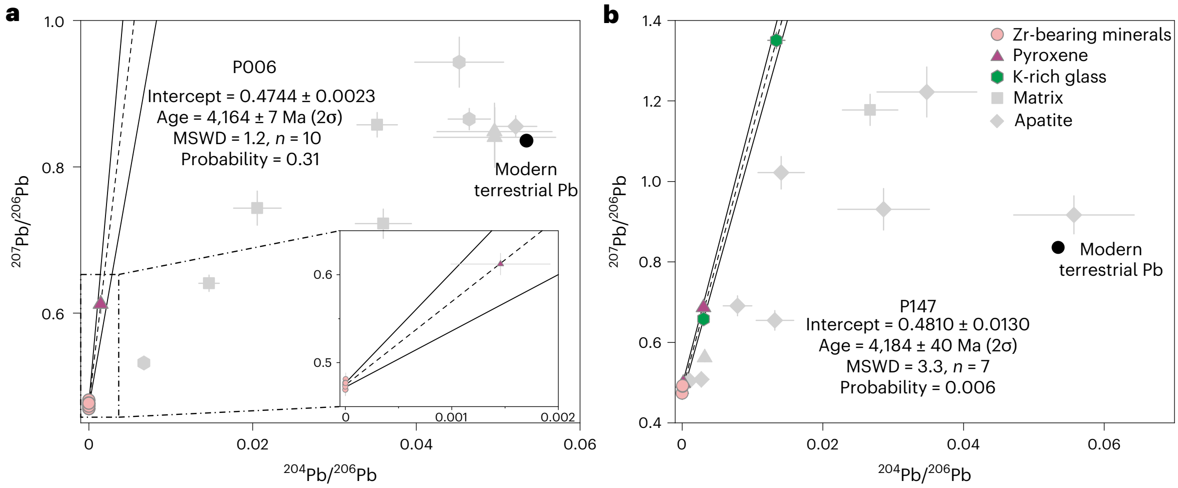

Fig. 4 | Pb–Pb plots of two CE-6 lithic fragments. a, A Pb–Pb isochron established form Zr-bearing minerals (zirconolite and baddeleyite), K-glass, intercumulus matrix (silica–K rich), apatite and pyroxene in P006. The insert shows an enlarged view of the bottom left corner of the main graph. **b**, A Pb–Pb isochron established form zircon, K-rich glass, apatite and pyroxene in P147. Data points shown in grey in both plots are excluded from the isochron age calculations owing to their proximity to terrestrial Pb values. Error bars in the figures represent 2σ. MSWD, mean square weighted deviation.

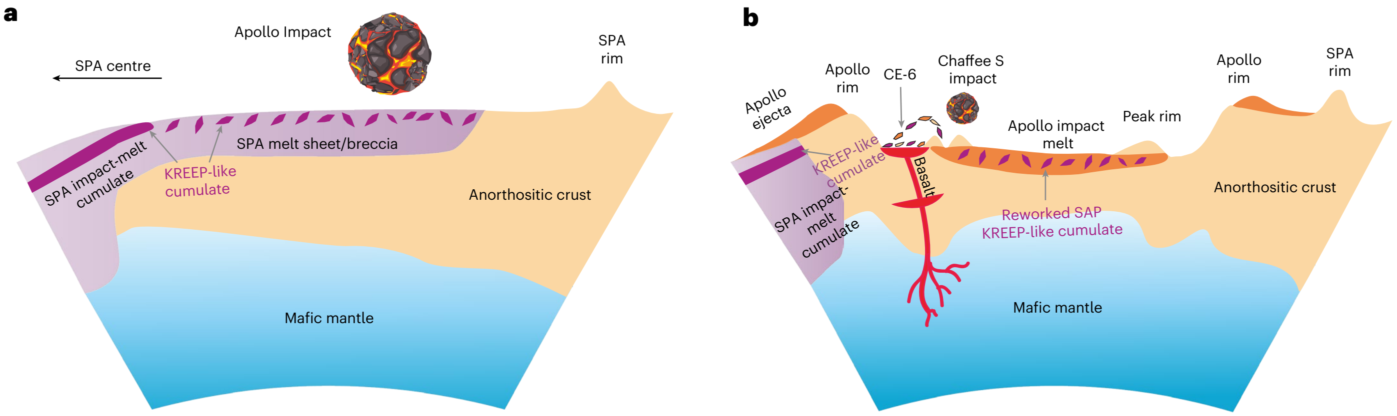

Stage I: Pre-Apollo impact basin

Stage II: Post-Apollo impact basin

Fig. 5 | Schematic diagram illustrates the two-stage origin of KREEP-like impact-melt fragments in the CE-6 regolith. a, When the SPA impact event occurred ~4.3 Ga (refs. 34,37), a large central Pre-Nectarian aged impact-melt pool was formed in the interior of the SPA basin. This melt pool possibly differentiated, resulting in a cumulate pile made of an ultramafic layer in the bottom and a noritic layer in the top with some evolved layers that probably had an enhanced ITE/KREEP-like geochemical signature[32]. **b**, At 4.16 Ga, the impactor that formed the Apollo basin impacted the periphery of the SPA basin impact-melt sheet, heating, melting and reworking this material. At <2.83 Ga (ref. 40), the Chaffee S impact within the Apollo basin could have delivered the KREEP-rich rocks formed by the Apollo impact to the CE-6 landing site.

probably represent the KREEP-rich SPA impact-melt differentiates or ejecta or the remelting of their precursors during the formation of Apollo basin. However, both sample analyses[34,37] and crater-counting studies[14] support the consensus that the age of the SPA basin is older than 4.2 Ga, bolstered by recent CE-6 sample results of impact-derived norite that suggest a SPA basin age of 4.25 Ga (ref. 38). Therefore, the younger impact-melt fragments analysed here are unlikely to represent the age of the SPA basin itself.

The preferred interpretation is that the precursor materials of CE-6 KREEP-rich impact melts were differentiates from the SPA impact-melt sheet that were remelted during the later formation of the Apollo basin[19] (Fig. 5). KREEP-like materials have been reported to overlie the area of the pre-Apollo impact basin[6,29,39]. Notably, the Apollo basin region shows lower concentrations of Th than its surroundings along the SPA topographic rim[29] (Extended Data Fig. 5), supporting the reworking of the KREEP-rich SPA impact-melt differentiates by the Apollo basin. A significant amount of Apollo basin impact-melt deposits[39], potentially including crystalline KREEP-rich rocks, is dispersed extensively in and around the vicinity of the basin. According to the prediction of ballistic sedimentation models[40], the majority of exotic (that is, non-local) materials in the CE-6 regolith should have been delivered by a large and proximal impact crater adjacent to the sampled unit. The CE-6 KREEP-like impact-melt fragments without intense secondary shock features indicate that they were not altered by multiple intense shock events, probably supporting an origin from a nearby impact crater.

The Chaffee S impact crater, located within the southwest rim of the Apollo basin (Extended Data Fig. 5a), may have transferred Apollo basin ejecta to the site sampled by the CE-6 mission[19] (Fig. 5b). Chaffee S ejecta, exhibiting low-Ca pyroxene spectral features, appears to overlie the CE-6 mare unit and would have been mixed into the local regolith[19]. This material is mineralogically consistent with the low-Ca pigeonite rich nature of two impact-melt fragments investigated here. Furthermore, the slightly elevated Th abundance (Extended Data Fig. 5b) of the Apollo basin western peak ring and Chaffee S ejecta[19] supports the idea that KREEP-like rocks occur close to the Apollo basin. Considering the small size (~20 km) and young age <2.8 Ga (ref. 41) of the Chaffee S impact crater, the ages of impact-melt fragments do not represent the age of this crater. As the CE-6 sampling site is situated on the surface of a young mare unit (~2.83 Ga)[20,21], these impact-melt fragments cannot be transported to their locations by an impact at 4.16 Ga. Furthermore, the Pb–Pb isotopic ages of the CE-6 impact-melt fragments are perfectly consistent with the model age (4.14$^{+0.024}_{-0.029}$ Ga) of the Apollo basin[14]. Therefore, we interpret the Pb–Pb age of 4.16 Ga dated for two of the CE-6 impact-melt fragments to represent the formation age of the Apollo basin.

Early lunar impact flux

The proposed isotopic age of the Apollo basin at 4.16 Ga here establishes an old sample-controlled calibration point for the lunar impact flux. This new calibration point is consistent with an extension of both the canonical Neukum crater chronology model[42] and the recently calibrated crater chronology model to older ages[20], showing that the early rapid decline in impact flux began at least as early as 4.16 Ga (Extended Data Fig. 6). Furthermore, the updated model age of the Apollo basin using crater statistics assumed that impactor populations on the Moon followed the same size-frequency distribution at least subsequent to the formation of the SPA basin[14].Therefore, the consistency between the isotopic age and model age of Apollo basin supports the interpretation that impactors on the Moon followed a similar size-frequency distribution at least since 4.16 Ga (refs. 14,17). Considering that the Apollo basin has a crater retention age slight younger than Nectaris basin[14], our proposed isotopic age of the Apollo basin also suggests that the Nectarian Period on the Moon started earlier than the canonically used 3.92 Ga, maybe slightly earlier than 4.16 Ga (ref. 9).

On the basis of spatial densities of impact crater populations formed on lunar terrains of different ages (Extended Data Fig. 7), there is a consensus that the early impact flux on the Moon was evidently orders of magnitude larger before 3.9 Ga (ref. 11) (Fig. 6). In relation to the stratigraphic position and the new isotopic age of the Apollo basin, 15 basins must have been formed separately in the Pre-Nectarian (that is, earlier than 4.16 Ga) and Nectarian to early Imbrian periods (that is, >4.16 Ga to ~3.8 Ga)[14]. Therefore, the LHB must have initiated before the Nectaris basin, that is, earlier than 4.16 Ga (ref. 11). If the SPA basin was indeed formed at ~4.3 Ga (refs. 14,34,37), 15 basins were formed within ~140 Ma between ~4.16 and 4.3 Ga and another 15 basins were formed in the subsequent 360 Ma (from 4.16 to 3.8 Ga), suggesting an even larger impact flux between the formation of SPA and Apollo. This first-order comparison agrees with a rapid decline of impact flux since the SPA basin-forming event, possibly even earlier since the Moon's formation[42]. Alternatively, if the SPA basin formed earlier

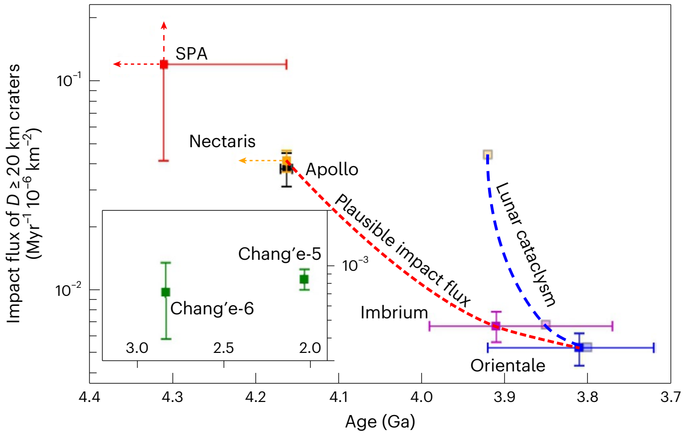

Fig. 6 | Synthesis of the early impact flux on the Moon. The inset figure shows the much smaller impact flux for craters larger than 20 km in diameter at the CE-5 and CE-6 landing sites. The ranges of ages and spatial densities of craters larger than 20 km in diameter for key impact basins are summarized in the Methods. Error bars with arrows are not to scale. Dashed red error bars with arrows denote the unconfirmed spatial density and isotopic age of the SPA basin. The dashed yellow error bar with arrows denotes that the Nectaris basin is older than 4.16 Ga. Solid squares and the dashed red line are the plausible impact flux derived from this work. Transparent squares and the dashed blue line are impact fluxes that assumed a cataclysm scenario of the LHB (Methods).

than ~4.3 Ga, for instance, at ~4.42 Ga when the oldest lunar zircon crystallized[43], the early impact flux between SPA and Apollo impacts would still be significantly higher, but to a lesser extent, than that between the Apollo and Orientale impacts. Nevertheless, if the SPA age is younger than ~4.3 Ga, for example, 4.25 (ref. 38), the impact flux during LHB declined much more rapidly before the Apollo basin was formed than afterwards (Fig. 6).

In any case, the isotopic age of the Apollo basin is not consistent with the scenario of a dramatic period of basin formation in a cataclysm between ~4.0 and 3.8 Ga (ref. 44) or even ~3.9–3.8 Ga (ref. 41). This interpretation reinforces the importance of acquiring a reliable formation age of the SPA basin, which is crucial for determining the impact flux during the LHB and the early evolution of our Solar System—for example, whether a late orbital reconfiguration of the giant planets occurred[45] and the evolution of small body reservoirs[46].

Methods

SEM and EBSD

Scanning electron microscopy (SEM) was used to take photos of minerals within epoxy sections at ~15 kV working voltage and with a suitable working distance. After the SEM observation, the epoxy samples were polished, using a VibroMet 2 vibratory polisher, for 3 h, and then deposited with a thin layer of carbon (~20 nm) using a Leica EM ACE600 sputtering coater to allow preferable electron back-scattered diffraction (EBSD) analyses. EBSD data were collected on a Thermofisher Helios CX5 dual beam system with an Oxford Aztec Symmetry II EBSD detector at the Electron Microscopy Center of GIGCAS (Guangzhou Institute of Geochemistry, Chinese Academy of Sciences). EBSD data collection was operated at 20 kV accelerating voltage and ~16.5 mm working distance. The step size ranged from 0.1 to 0.3 µm. ATEX software was adopted for post-data processing and the creation of interest maps. Phase maps identified by EBSD were used to estimate mineral modes. (Supplementary Table 1).

Field-emission electron microprobe for major element compositions of minerals

The elemental concentrations of silicate, oxide, glass and Fe–Ni metal were determined using a CAMECA SX5 field-emission electron microprobe (EMP) at the State Key Laboratory of Deep Earth Processes and Resources (SKLDEEPER), GIGCAS. This instrument is equipped with five wavelength-dispersive X-ray spectrometers and incorporates a total of 14 crystals installed within 160-mm-radius Rowland circles. A detailed description of this EPM procedure can be found in ref. 47. The analysis was conducted using an accelerating voltage of 15 kV, a beam current of 20 nA and a beam size of 1 µm. For the slim high-Ca augite (~1 µm) exsolved in the low-Ca pigeonite, we obtain their mixing compositions. A variable peak counting time (~10–100 s) was used based on the intensity of the characteristic X-ray line and desired precision for the major oxides. The background counting time was set to half of the peak counting time on both sides of peak. Calibration standards include albite (Na), diopside (Si, Ca, Mg), haematite/pyrite (Fe), sanidine (K), almandine (Al), rutile (Ti), chromite (Cr), rhodonite (Mn), pentlandite (Ni), metal cobalt (Co) and synthetic RbTiPO5 (P). The corresponding standard materials were selected according to the target minerals. For example, the plagioclase standard was used for Si, Ca and Al analyses on plagioclase, while the glass standard BIR-1G was employed for Si, Ca, Mg, Al and Fe analyses on glass. The metal standard was selected to analyse the Fe–Ni metal. Finally, a Pouchou and Pichoir (PAP) procedure was used for matrix correction. Full EMP data are available in Source Data Fig. 2.

Calculation of REE concentrations of melts in equilibrium with plagioclase and pigeonite

The partition coefficients (*D*) of REE in plagioclase and pigeonite have been reported by Dygert et al.[48], who conducted a series of experiments under near-lunar conditions. REE concentrations in melts in equilibrium with plagioclase was calculated using *D* (plagioclase): La (0.0245), Ce (0.02), Pr (0.0176), Nd (0.0165), Sm (0.0115), Eu (0.8491), Gd (0.0082), Tb (0.0061), Dy (0.005), Ho (0.004), Er (0.0031), Tm (0.0026), Yb (0.0034) and Lu (0.0017). The pyroxenes investigated in this study are pigeonite, despite having exsolved textures. Thus, we selected the *D* (pigeonite) to estimate the REE in melts in equilibrium with pyroxenes, specifically: La (0.0053), Ce (0.0079), Pr (0.013), Nd (0.019), Sm (0.04), Eu (0.067), Gd (0.07), Tb (0.093), Dy (0.111), Ho (0.133), Er (0.151), Tm (0.169), Yb (0.184) and Lu (0.205).

LA-SF-ICP-MS for measurement of mineral trace element compositions

Trace element contents of pyroxene and plagioclase were determined with an ELEMENT XR (Thermo Fisher Scientific) sector field (SF) inductively coupled plasma mass spectrometer (ICP-MS) coupled to a 193-nm (ArF) Resonetics RESOlution M-50 laser ablation (LA) system. The laser conditions were as follows: 6 Hz repetition rate for all analyses; 33/24/17 µm beam size was used depending on sample sizes. Each analysis consisted of 30 s gas blank collection and 29 s sample data acquisition. The oxide molecular yield (indicated by $^{232}\mathrm{Th}^{16}\mathrm{O}/^{232}\mathrm{Th}$) was <0.3%. Signals of the following masses were measured: ^{238}U, ^{232}Th, ^{208}Pb, ^{181}Ta, ^{178}Hf, ^{175}Lu, ^{174}Yb, ^{169}Tm, ^{166}Er, ^{165}Ho, ^{162}Dy, ^{159}Tb, ^{157}Gd, ^{151}Eu, ^{147}Sm, ^{146}Nd, ^{141}Pr, ^{140}Ce, ^{139}La, ^{137}Ba, ^{93}Nb, ^{90}Zr, ^{89}Y, ^{88}Sr, ^{85}Rb and ^{29}Si. The calibration lines for the analysed element were constructed by measuring two reference glasses (BHVO-2G and GSD-1G). Silicon, premeasured with EPM, was selected as the internal standard element. Given that the intercumulus liquid is too small to directly analyse the trace elements, a relatively large laser beam (33 µm) was used to ablate the intercumulus liquid and the tiny matrix plagioclase together on sample S3583-P006 (Supplementary Fig. 1). All major elements and selected trace elements were detected (Source Data Fig. 3). The final content of each element of the mixture was calculated by normalizing all the measured element oxides to 100 wt.%. The trace element composition of the intercumulus liquid was calculated using a mass balance model. Based on the average K_2O contents of plagioclase and the intercumulus liquid measured by EPMA, the estimated plagioclase proportion in the mixture of the intercumulus liquid and the tiny matrix plagioclase is

72%. Then, the trace element contents of the intercumulus liquid were calculated by subtracting the contribution of the ablated plagioclase from the mixture. Geological reference glass BCR-2G was measured as an unknown sample to evaluate data quality. The detailed instrumental settings and data reduction strategies are reported in ref. 49. For most measured elements, the accuracy is better than ±10% with an analytical precision of better than 10%.

In situ Rb–Sr isotope measurements by LA-MC-ICP-MS

In situ Rb–Sr isotope analyses were conducted on a Neptune Plus multiple-collector (MC) ICP-MS (Thermo Scientific), coupled with the same LA system used for trace element analysis at SKLDEEPER, GIGCAS. The laser parameters were as follows: a beam diameter of 112 μm, a repetition rate of 15 Hz and an energy density of ~4.5 J cm^{-2}. Under this laser set-up, all the measured CE-6 samples had ^{88}Sr signal intensities larger than 0.7 V. The isobaric interferences (^{86}Kr and ^{84}Kr on ^{86}Sr and ^{84}Sr) were corrected by subtracting gas blank from the raw time-resolved signal intensities. The signals at 83.5 and 85.5 were used to monitor double-charged ^{167}Er^{2+} and ^{171}Yb^{2+}, which were then used to correct the interferences of Er^{2+} and Yb^{2+}. The interference of ^{87}Rb on ^{87}Sr was corrected with the measured ^{85}Rb with a natural ^{85}Rb/^{87}Rb = 2.593 (ref. 50). The mass bias of ^{87}Sr/^{86}Sr was calibrated by normalizing ^{86}Sr/^{88}Sr to 0.1194 with an exponential law. The detailed instrumental set-up and data reduction procedure were reported in previous studies[51,52]. ^{87}Rb/^{86}Sr was calibrated with the standard-sample-bracketing method with BCR-2G (a geological reference glass) used as an external calibrator. The analytical reproducibility of ^{87}Rb/^{86}Sr, evaluated by repeating analysis of BHVO-2G (0.5%, $n = 3$), was propagated to the uncertainty of ^{87}Rb/^{86}Sr of the measured samples. Three analyses of BHVO-2G and BCR-2G during this study yielded averaged ^{87}Sr/^{86}Sr = 0.70348 ± 0.00008 (2 s.d.) and 0.70502 ± 0.00007 (2 s.d.), respectively, which are consistent within error with their recommended values[53]. Four analyses of an in-house plagioclase glass (PZHPL, An = 56) yielded weighted means of ^{87}Sr/^{86}Sr = 0.70437 ± 0.00005 (2 s.d.), which agrees within error with the result measured by solution MC-ICP-MS[54]. The analytical uncertainty of isotopic data is given as 2σ (Source Data Fig. 3).

In situ Pb isotope analyses by SIMS

All Pb–Pb data were acquired by the CAMECA-IMS-1280-HR secondary-ion mass spectrometer (SIMS) at SKLDEEPER, GIGCAS, Guangzhou. To obtain high ion-beam density (the maximum intensity of the ^{16}O^{-} primary beam is approximately 3.0 μA), we followed the instrument settings in ref. 55, including adding plasma arc current up to the designed maximum limit of about 100 mA and using a modified duoplasmatron cathode. A Gaussian illumination mode was used to focus a primary beam of ^{16}O^{-} to 2 × 3 μm in size, with an intensity of 210–365 pA. Beam diameter was measured using the knife-edge method of SpotShape software and reconfirmed by obtaining an ion image on an area with a 2–3-μm-spaced raster pattern. Five low-noise (<0.003 counts per second) electronic multipliers (Hamamatsu 416) were used to simultaneously collect ions of ^{208}Pb, ^{207}Pb, ^{206}Pb and ^{204}Pb, under the multicollector mode. Entrance (60 μm) and exit (150 μm) slits were adjusted to obtain a mass resolution of ~8,000 (50% peak height). A nuclear magnetic resonance controller was used to keep a stable magnetic field, with an instrumental drift of <1.5 ppm over 1 h. Before each measurement, a primary beam of ^{16}O^{-} with an intensity of 8 nA was used for 120 s to remove the gold coating and minimize possible surface contamination. The ion images of ^{90}Zr^{+} on a ~25 μm × 25 μm area were used to precisely locate the target minerals. Each measurement consisted of 4 s × 80 cycles. High-purity oxygen flooding was introduced to the sample surface to improve Pb^{+} sensitivity. Geological reference glass, NIST 610, was used to calculate the relative yield of different electronic multipliers and evaluate the external reproducibility, yielding precisions of ^{208}Pb/^{206}Pb = 0.55%, ^{207}Pb/^{206}Pb = 0.71% and ^{204}Pb/^{206}Pb = 2.69% (reported as 1 relative standard (RSD), $n = 32$). The uncertainties on each unknown analysis were propagated to determine the overall uncertainties of single spot analysis. Within uncertainty limits, no systematic drift was observed in the NIST 610 measurements during a given analytical session. A baddeleyite standard Phalaborwa (^{207}Pb*/^{206}Pb* = 0.1272 (ref. 56)) was measured as an unknown sample at two sessions to monitor the correction factor and data processing.

The Pb isotopic compositions of apatite, K-rich glass, matrix and pyroxene were determined using a CAMECA-IMS-1280-HR SIMS equipped with an updated Radio Frequency oxygen source in the Institute of Geology and Geophysics, Chinese Academy of Sciences (IGGCAS) in Beijing. The primary beam sizes of 5, 10 and 30 μm with intensities of ~170 pA, ~6 nA and 20 nA were selected according to size of minerals to minimize terrestrial lead introduced from cracks and mineral boundaries. SIMS analytical locations on two repolished sections are marked in Supplementary Fig. 2. Multicollector mode with four electric multipliers (EMs) was used to measure ^{204}Pb + (L2), ^{206}Pb^{+} (C), ^{207}Pb^{+} (H1) and ^{96}Zr^{216}O^{2+} (H2). Before each measurement, an area of 20 μm around the spot location was raster-scanned for 120 s to remove the gold coating and minimize possible surface contamination. Other procedures and data processing methods are the same as those of the SIMS laboratory in GIGCAS. All SIMS datasets are included in Source Data Fig. 4. Ultimately, data affected by terrestrial contamination were filtered out to calculate the Pb–Pb age of the sample, following the protocol established in previous studies[57,58].

The *N*(1) value of the Apollo basin

To establish a new calibration point for impact flux using the isotopic age of the Apollo basin, a representative production density of impact craters that were formed in the Apollo basin is needed. Canonically, the number of craters equal to and larger than 1 km in diameter per square kilometre, *N*(1), is used as the representative production density[59]. However, the Apollo basin is a Nectarain- or Early-Imbrian-aged basin that has undergone prolonged postformation resurfacing and contamination by kilometre-scale secondaries[14], which have prohibited direct extraction of *N*(1) based on the observed population of craters larger than 1 km in diameter (*D*). Typically, a crater production function that describes the densities of different-sized craters formed in a given period is needed to derive *N*(1) from larger or smaller diameter ranges. Recent crater statistics for the Apollo basin derived size-frequency distribution of craters with $D \geq 20$ km after considering the effect of non-sparseness of densely packed craters, which may have caused disproportionately removal of differently sized earlier craters[14]. Using the corrected crater size-frequency distribution and the Neukum crater production and chronology functions[59], the predicted model age for the Apollo basin was 4.14 (+0.024, −0.029), which is closely consistent with the isotopic age derived in this work. It is notable that, by applying the same crater production and chronology functions[59], the first-order consistency between model ages and isotopic ages has been repeatedly verified, such as the Chang'e-5[60] and CE-6[20] landing site mare deposits. Therefore, following the recommendation that the model age of Apollo is better modelled using the crater size-frequency distribution at $D \geq 20$ km (ref. 14), the *N*(1) value and its associated errors are derived using the reported model age and the Neukum crater chronology model[59]. The result is shown in Extended Data Fig. 6 (red dot). Notably, this study did not try to recalibrate the crater chronology model using the new calibration point of the Apollo basin, because the *N*(1) value—calculated from the best-fit model age—yielded an *N*(20) via the Neukum production function that differed from the directly observed *N*(20). This discrepancy suggests that deriving *N*(1) using the canonical production function may involve notable uncertainties. Nevertheless, the new calibration point of the Apollo basin falls directly on both the canonical and updated crater chronology models (Extended Data Fig. 6), suggesting that these models and the related impact flux can be used together with crater statistics to estimate model ages up to at least 4.16 Ga.

Evaluation of the early impact flux on the Moon

To evaluate the impact flux during LHB (that is, between the formation of SPA and the Orientale basins), the formation ages and representative production densities of critical basins are needed. The SPA, Nectaris, Imbrium and Orientale basins are undisputedly critical basins for this purpose, and their formation ages largely determine the impact flux during LHB[11,12]. For Nectarian- and Imbrian-aged basins, the effect of crater non-sparseness due to dense packing is relatively minor when deriving the production population, and the $N(20)$ values obtained after accounting for this effect remain reasonably reliable[14]. Therefore, in this work, we refer to these $N(20)$ values and their errors[14] for the Nectaris, Imbrium and Orientale basins (Extended Data Fig. 7), and the impact flux during LHB is represented by the formation rate of craters larger than 20 km in diameter per million square kilometres per million years (Extended Data Fig. 6).

By contrast, the cratering record superposed on pre-Nectarian basins, especially the SPA basin, is significantly biased due to the effect of non-sparseness, and extracting their $N(20)$ values is hampered by uncertainties caused by crater equilibrium[14,17]. This effect is most obvious for crater populations formed in the SPA basin, as its reported $N(20)$ value is only slightly larger than that of the Nectaris basin[14]. Therefore, using the best-fit model age of the SPA basin (that is, 4.33 Ga)[14], which is also supported by recent sample analyse[34,37], the Neukum crater chronology and production models[59] are used to estimate the best-fit $N(20)$. For the error of this model-predicted $N(20)$, we consider that the actual production density of $N(20)$ should be larger than Nectaris, but the upper limit of $N(20)$ is not known. Therefore, the dashed red arrows in Extended Data Fig. 7 show the $N(20)$ and errors of the SPA basin.

The isotopic age of the Apollo basin establishes a clear reference for the possible impact flux during LHB. Isotopic ages of the SPA, Nectaris, Imbrium and Orientale basins are not well constrained; the Imbrium basin has a smaller range of uncertainties from ~3.85 to 3.92 Ga (ref. 61). The preferred formation age of Imbrium is plotted as 3.91 Ga (ref. 62), and the possible age range reported by sample analyses is 3.77–3.99 Ga (ref. 14) (Extended Data Fig. 7). The possible formation age of the Orientale basin that was derived from the non-sparseness-corrected crater size-frequency distribution (that is, 3.81 Ga (ref. 14)) was plotted (Extended Data Fig. 7), and the possible age range reported by earlier crater statistics is ~3.72–3.92 Ga (ref. 63). The Nectaris basin is probably older than 4.16 Ga, and it should be younger than the SPA basin. However, the precise age of the Nectaris basin is not known, and this uncertainty is marked as an orange arrow (Extended Data Fig. 7). Likewise, while an age of 4.33 Ga is plotted in Extended Data Fig. 7 for the SPA basin (red square), the actual age might be much larger or smaller, but definitely larger than 4.16 Ga (Extended Data Fig. 7, dashed red arrows).

The impact flux during the LHB is investigated using the above ranges of formation ages and $N(20)$ of the four critical basins (Fig. 6, solid squares). The data are compared with a classic version of the late cataclysm[11], which assumed that the $N(20)$ values of the Nectaris, Imbrium and Orientale basins are the same as reported above (Extended Data Fig. 7), but they were formed at 3.92, 3.85 and 3.8 Ga, respectively (Fig. 6, transparent squares). To show qualitatively the contrast of impact flux during LHB, the dashed red and blue curves are annotated for the two versions of impact flux at these critical impact basins (Fig. 6)

Data availability

The CE-6 sample involved in this work was allocated by the Chinese National Space Administration (CNSA) under a materials transfer agreement (www.cnsa.gov.cn/n6758823/n6758839/c6811124/content.html). The prepared sample mounts are presently stored at GIGCAS, and they will be returned to CNSA after a 1-year loan. Readers may request Chang'e-6 samples from CNSA through a standard procedure. All data presented in this study are available in the Article and its source data. Source data are provided with this paper.

References

1. Shearer, C. et al. Magmatic evolution II: a new view of post-differentiation magmatism. *Rev. Mineral. Geochem.* **89**, 147–206 (2023).
2. Korotev, R. L. The great lunar hot spot and the composition and origin of the Apollo mafic ("LKFM") impact-melt breccias. *J. Geophys. Res. Planets* **105**, 4317–4345 (2000).
3. Warren, P. H. The magma ocean concept and lunar evolution. *Annu. Rev. Earth Planet. Sci.* **13**, 201–240 (1985).
4. Jolliff, B. L., Gillis, J. J., Haskin, L. A., Korotev, R. L. & Wieczorek, M. A. Major lunar crustal terranes: surface expressions and crust-mantle origins. *J. Geophys. Res. Planets* **105**, 4197–4216 (2000).
5. Zhang, N. et al. Lunar compositional asymmetry explained by mantle overturn following the South Pole–Aitken impact. *Nat. Geosci.* **15**, 37–41 (2022).
6. Moriarty, D. & Pieters, C. The character of South Pole–Aitken basin: patterns of surface and subsurface composition. *J. Geophys. Res. Planets* **123**, 729–747 (2018).
7. Jolliff, B. L. et al. Non-mare silicic volcanism on the lunar farside at Compton–Belkovich. *Nat. Geosci.* **4**, 566–571 (2011).
8. Uemoto, K. et al. Evidence of impact melt sheet differentiation of the lunar South Pole–Aitken basin. *J. Geophys. Res. Planets* **122**, 1672–1686 (2017).
9. Osinski, G. R. et al. Lunar impact features and processes. *Rev. Mineral. Geochem.* **89**, 339–371 (2023).
10. Wetherill, G. Late heavy bombardment of the moon and terrestrial planets. In *6th Annual Lunar and Planetary Science Conference* 1539–1561 (Lunar and Planetary Institute, 1975).
11. Bottke, W. F. & Norman, M. D. The late heavy bombardment. *Annu. Rev. Earth Planet. Sci.* **45**, 619–647 (2017).
12. Fassett, C. I. & Minton, D. A. Impact bombardment of the terrestrial planets and the early history of the Solar System. *Nat. Geosci.* **6**, 520–524 (2013).
13. Snape, J. F. et al. Post-Imbrium Pb–Pb isochron ages for Apollo basaltic impact melt samples 14078 and 68415. *R. Soc. Open Sci.* **11**, 231963 (2024).
14. Orgel, C. et al. Ancient bombardment of the inner solar system: reinvestigation of the "fingerprints" of different impactor populations on the lunar surface. *J. Geophys. Res. Planets* **123**, 748–762 (2018).
15. Spudis, P. D. Apollo 16 site geology and impact melts: Implications for the geologic history of the lunar highlands. *J. Geophys. Res. Solid Earth* **89**, C95–C107 (1984).-
16. Warren, P. H. The Moon. In *Treatise on Geochemistry* 559–599 (Elsevier, 2003).
17. Fassett, C. et al. Lunar impact basins: stratigraphy, sequence and ages from superposed impact crater populations measured from Lunar Orbiter Laser Altimeter (LOLA) data. *J. Geophys. Res. Planets* **117**, E00H06 (2012).
18. Hiesinger, H. et al. The lunar cratering chronology. *Rev. Mineral. Geochem.* **89**, 401–451 (2023).
19. Qian, Y. et al. Extensive intrusive magmatism in the lunar farside Apollo and South Pole–Aitken Basins, Chang'e-6 landing site. *Astrophys. J. Lett.* **971**, L39 (2024).
20. Cui, Z. et al. A sample of the Moon's far side retrieved by Chang'e-6 contains 2.83-billion-year-old basalt. *Science* **368**, 1395–1399 (2024).
21. Zhang, Q. W. et al. Lunar farside volcanism 2.8 billion years ago from Chang'e-6 basalts. *Nature* **643**, 356–360 (2025).
22. Walker, D., Powell, M., Lofgren, G. E. & Hays, J. Dynamic crystallization of a eucrite basalt. In *9th Annual Lunar and Planetary Science Conference* 1369–1391 (Lunar and Planetary Institute, 1978).

23. Jolliff, B., Floss, C., McCallum, I. & Schwartz, J. Geochemistry, petrology, and cooling history of 14161, 7373: a plutonic lunar sample with textural evidence of granitic-fraction separation by silicate-liquid immiscibility. *Am. Miner.* **84**, 821–837 (1999).
24. Takeda, H., Mori, H., Ishii, T. & Miyamoto, M. Thermal and impact histories of pyroxenes in lunar eucrite-like gabbros and eucrites. In *12th Annual Lunar and Planetary Science Conference* 1297–1313 (Lunar and Planetary Institute, 1982).
25. Cronberger, K. & Neal, C. R. KREEP basalt petrogenesis: insights from 15434,181. *Meteorit. Planet. Sci.* **52**, 827–841 (2017).
26. Fagan, T. J., Kashima, D., Wakabayashi, Y. & Suginohara, A. Case study of magmatic differentiation trends on the Moon based on lunar meteorite Northwest Africa 773 and comparison with Apollo 15 quartz monzodiorite. *Geochim. Cosmochim. Acta* **133**, 97–127 (2014).
27. Neal, C. & Kramer, G. The composition of KREEP: a detailed study of KREEP basalt 15386. In *34th Annual Lunar and Planetary Science Conference* 2023 (Lunar and Planetary Institute, 2003).
28. Reimold, W. et al. Isotope analysis of crystalline impact melt rocks from Apollo 16 stations 11 and 13, North Ray Crater. *J. Geophys. Res. Solid Earth* **90**, C431–C448 (1985).
29. Moriarty, D. et al. Evidence for a stratified upper mantle preserved within the South Pole–Aitken basin. *J. Geophys. Res. Planets* **126**, e2020JE006589 (2021).
30. Haskin, L. A., Korotev, R. L., Rockow, K. M. & Jolliff, B. L. The case for an Imbrium origin of the Apollo thorium-rich impact-melt breccias. *Meteorit. Planet. Sci.* **33**, 959–975 (1998).
31. Garrick-Bethell, I. & Zuber, M. T. An indigenous origin for the South Pole Aitken basin thorium anomaly. *Geophys. Res. Lett.* **32**, L13203 (2005).
32. Vaughan, W. M. & Head, J. W. Impact melt differentiation in the South Pole–Aitken basin: some observations and speculations. *Planet. Space Sci.* **91**, 101–106 (2014).
33. Wang, X. et al. Lunar farside South Pole–Aitken basin interior: evidence for more extensive central cryptomaria in the South Pole–Aitken compositional anomaly (SPACA). *J. Geophys. Res. Planets* **129**, e2023JE008176 (2024).
34. Joy, K. et al. Evidence of a 4.33 billion year age for the Moon's South Pole–Aitken basin. *Nat. Astron.* https://doi.org/10.1038/s41550-024-02380-y (2024).
35. Melosh, H. et al. South Pole–Aitken basin ejecta reveal the Moon's upper mantle. *Geology* **45**, 1063–1066 (2017).
36. Zhang, Y. et al. The very late-stage crystallization of the lunar magma ocean and the composition of immiscible urKREEP. *Earth Planet. Sci. Lett.* **646**, 118989 (2024).
37. Barboni, M. et al. High-precision U–Pb zircon dating identifies a major magmatic event on the Moon at 4.338 Ga. *Sci. Adv.* **10**, eadn9871 (2024).
38. Su, B. et al. South Pole–Aitken massive impact 4.25 billion years ago revealed by Chang'e-6 samples. *Natl Sci. Rev.* **12**, nwaf103 (2025).
39. Potter, R. W., Head, J. W., Guo, D., Liu, J. & Xiao, L. The Apollo peak-ring impact basin: Insights into the structure and evolution of the South Pole–Aitken basin. *Icarus* **306**, 139–149 (2018).
40. Xu, L. et al. Chronology, local stratigraphy, and foreign ejecta materials at the Chang'e-6 landing site: constraints on the provenance of samples returned from the Moon's farside. *Geophys. Res. Lett.* **51**, e2024GL111311 (2024).
41. Ryder, C. Lunar samples, lunar accretion and the early bombardment of the Moon. *Trans. Am. Geophys. Union* **71**, 313–323 (1990).
42. Neukum, G., Ivanov, B. A. & Hartmann, W. K. Cratering records in the inner Solar System in relation to the lunar reference system. *Space Sci. Rev.* **96**, 55–86 (2001).
43. Nemchin, A. et al. Timing of crystallization of the lunar magma ocean constrained by the oldest zircon. *Nat. Geosci.* **2**, 133–136 (2009).
44. Tera, F., Papanastassiou, D. A. & Wasserburg, G. J. Isotopic evidence for a terminal lunar cataclysm. *Earth Planet. Sci. Lett.* **22**, 1–21 (1974).
45. Morbidelli, A. et al. The timeline of the lunar bombardment: revisited. *Icarus* **305**, 262–276 (2018).
46. Brasser, R., Werner, S. & Mojzsis, S. Impact bombardment chronology of the terrestrial planets from 4.5 Ga to 3.5 Ga. *Icarus* **338**, 113514 (2020).
47. He, P.-L., Huang, X.-L., Yang, F. & Wang, X. Mineralogy constraints on magmatic processes controlling adakitic features of Early Permian high-magnesium diorites in the Western Tianshan orogenic belt. *J. Petrol.* **61**, egaa114 (2020).
48. Dygert, N. et al. Experimental determinations of trace element partitioning between plagioclase, pigeonite, olivine, and lunar basaltic melts and an fO_2 dependent model for plagioclase-melt Eu partitioning. *Geochim. Cosmochim. Acta* **279**, 258–280 (2020).
49. Zhang, L. et al. In situ determination of trace elements in melt inclusions using laser ablation inductively coupled plasma sector field mass spectrometry. *Rapid Commun. Mass Spectrom.* **33**, 361–370 (2019).
50. Rosman, K. J. R. & Taylor, P. D. P. Isotopic compositions of the elements 1997. *Pure Appl. Chem.* **70**, 217–235 (1998).
51. Zhang, L., Ren, Z.-Y., Wu, Y.-D. & Li, N. Strontium isotope measurement of basaltic glasses by laser ablation multiple collector inductively coupled plasma mass spectrometry based on a linear relationship between analytical bias and Rb/Sr ratios. *Rapid Commun. Mass Spectrom.* **32**, 105–112 (2018).
52. Zhang, L., Ren, Z.-Y., Xia, X.-P., Li, J. & Zhang, Z.-F. IsotopeMaker: a Matlab program for isotopic data reduction. *Int. J. Mass Spectrom.* **392**, 118–124 (2015).
53. Elburg, M., Vroon, P., van der Wagt, B. & Tchalikian, A. Sr and Pb isotopic composition of five USGS glasses (BHVO-2G, BIR-1G, BCR-2G, TB-1G, NKT-1G). *Chem. Geol.* **223**, 196–207 (2005).
54. Zhang, L. et al. The origins of high-Ti and low-Ti magmas in large igneous provinces, insights from melt inclusion trace elements and Sr–Pb isotopes in the Emeishan large Igneous Province. *Lithos* **344-345**, 122–133 (2019).
55. Liu, Y., Li, X. H., Li, Q. L. & Tang, G. Q. Breakthrough of 2- to 3-μm scale U–Pb zircon dating using Cameca IMS-1280HR SIMS. *Surf. Interface Anal.* **52**, 214–223 (2020).
56. Reischmann, T. Precise U/Pb age determination with baddeleyite (ZrO_2), a case study from the Phalaborwa igneous complex. *S. Afr. J. Geol.* **98**, 1–4 (1995).
57. Snape, J. F. et al. Lunar basalt chronology, mantle differentiation and implications for determining the age of the Moon. *Earth Planet. Sci. Lett.* **451**, 149–158 (2016).
58. Merle, R. E. et al. Pb–Pb ages and initial Pb isotopic composition of lunar meteorites: NWA 773 clan, NWA 4734, and Dhofar 287. *Meteorit. Planet. Sci.* **55**, 1808–1832 (2020).
59. Neukum, G. Meteoriten Bombardement und Datierung Planetarer Oberflachen. PhD thesis (Ludwig-Maximilians University, 1983).
60. Li, Q.-L. et al. Two-billion-year-old volcanism on the Moon from Chang'e-5 basalts. *Nature* **600**, 54–58 (2021).
61. Stöffler, D. & Ryder, G. Stratigraphy and isotope ages of lunar geologic units: chronological standard for the inner Solar System. *Space Sci. Rev.* **96**, 9–54 (2001).
62. Liu, D. et al. Comparative zircon U–Pb geochronology of impact melt breccias from Apollo 12 and lunar meteorite SaU 169, and implications for the age of the Imbrium impact. *Earth Planet. Sci. Lett.* **319-320**, 277–286 (2012).

63. Werner, S. & Ivanov, B. Exogenic dynamics, cratering, and surface ages. In *Treatise on Geophysics* 327–365 (Elsevier, 2015); https://doi.org/10.1016/B978-0-444-53802-4.00170-6
64. Marvin, U., Lindstrom, M., Holmberg, B. & Martinez, R. New observations on the quartz monzodiorite-granite suite. In *21st Lunar and Planetary Science Conference* 119–135 (Lunar and Planetary Institute, 1990).
65. Wieczorek, M. A. et al. The constitution and structure of the lunar interior. *Rev. Mineral. Geochem.* **60**, 221–364 (2006).
66. Shearer, C. K., Elardo, S. M., Petro, N. E., Borg, L. E. & McCubbin, F. M. Origin of the lunar highlands Mg-suite: an integrated petrology, geochemistry, chronology, and remote sensing perspective. *Am. Miner.* **100**, 294–325 (2015).
67. Jolliff, B. Fragments of quartz monzodiorite and felsite in Apollo 14 soil particles. In *21st Annual Lunar and Planetary Science Conference* 101–118 (Lunar and Planetary Institute, 1990).
68. Day, J. M. D. Metal grains in lunar rocks as indicators of igneous and impact processes. *Meteorit. Planet. Sci.* **55** https://doi.org/10.1111/maps.13544 (2020).
69. Papike, J. J., Fowler, G. W. & Shearer, C. K. Orthopyroxene as a recorder of lunar crust evolution: an ion microprobe investigation of Mg-suite norites. *Am. Miner.* **79**, 796–800 (1994).
70. Palme, H. & Jones, A. *Solar System Abundances of the Elements* (Elsevier, 2003); https://doi.org/10.1016/B0-08-043751-6/08126-3
71. Zhang, L. et al. Elemental and Sr isotopic compositions of plagioclase as an indicator of lunar source-rock type: insights from Chang'e 5 plagioclase fragments. *Icarus* **413**, 116002 (2024).
72. Potter, R. W., Collins, G. S., Kiefer, W. S., McGovern, P. J. & Kring, D. A. Constraining the size of the South Pole–Aitken basin impact. *Icarus* **220**, 730–743 (2012).
73. Qiao, L. et al. Geology of the Chang'e-5 landing site: constraints on the sources of samples returned from a young nearside mare. *Icarus* **364**, 114480 (2021).
74. Hiesinger, H. et al. How old are young lunar craters? *J. Geophys. Res. Planets* **117**, E00H10 (2012).

Acknowledgements

We thank the China National Space Administration (CNSA) for providing the CE-6 samples. We thank the lunar working group at GIGCAS for inspiring discussions. We thank Q. Li and Y. Liu at IGGCAS for their assistance with SIMS test and data analysis. This study is financially supported by Chinese Academy of Sciences (ZDBS-SSW-JSC007-11, XDB 1180000), Lunar Research Program of GIGCAS (no. 2022SZJJZD-03), Bureau of Frontier Sciences and Basic Research, Chinese Academy of Sciences, (grant nos. QYJ-2025-0104 and QYJ-2025-0102) and the National Natural Science Foundation of China (grant no. 42241104). Y.Q. is funded by the HK RGC General Research Fund (17307025) and Co-funding Mechanism on Joint Laboratories with the Chinese Academy of Science (JLFS/P-702/24). K.H.J. is funded by the Royal Society (URF\R\201009 and URF\ERE\210158) and STFC (ST/V000675/1 and ST/Y002318/1).

Author contributions

Y.-G.X. designed the project. Y.-Q.Z. and J.C. prepared the sample mounts. L.Z., Z. Cui, Q.Y., Z. Chen, H.X., C.W., J.C., P.H., F.H. and L.C. collected analytical data. J.C., L.Z., Z. Cui and Z. Chen, produced tables and figures and performed calculations. J.C., Y.-G.X., L.Z., Z. Cui, Y.Q. and Z.X., wrote the draft manuscript. All authors reviewed and edited the manuscript.

Competing interests

We declare no competing interests.

Additional information

Extended data is available for this paper at https://doi.org/10.1038/s41550-025-02640-5.

Supplementary information The online version contains supplementary material available at https://doi.org/10.1038/s41550-025-02640-5.

Correspondence and requests for materials should be addressed to Yi-Gang Xu.

Peer review information *Nature Astronomy* thanks Renaud Merle and the other, anonymous, reviewer(s) for their contribution to the peer review of this work.

Reprints and permissions information is available at www.nature.com/reprints.

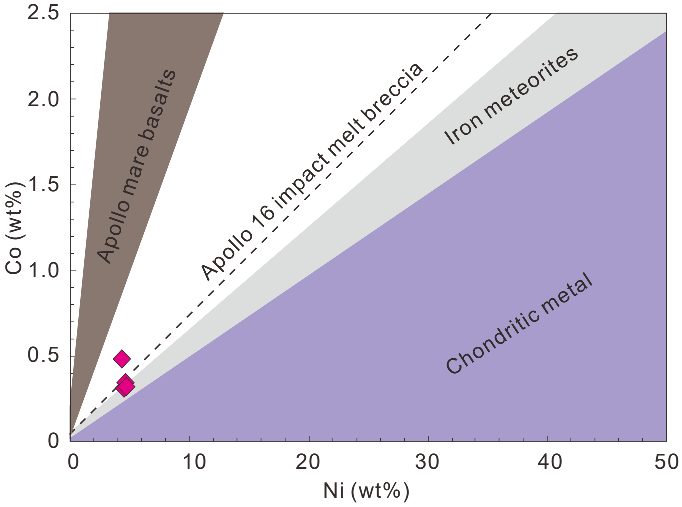

Extended Data Fig. 1 | Co versus Ni contents of FeNi alloy in the P106 fragment. The areas of Apollo mare basalts, iron meteorite, chondritic metal and the regression line of Apollo 16 impact melt breccia samples are from the compilation of ref. 68.

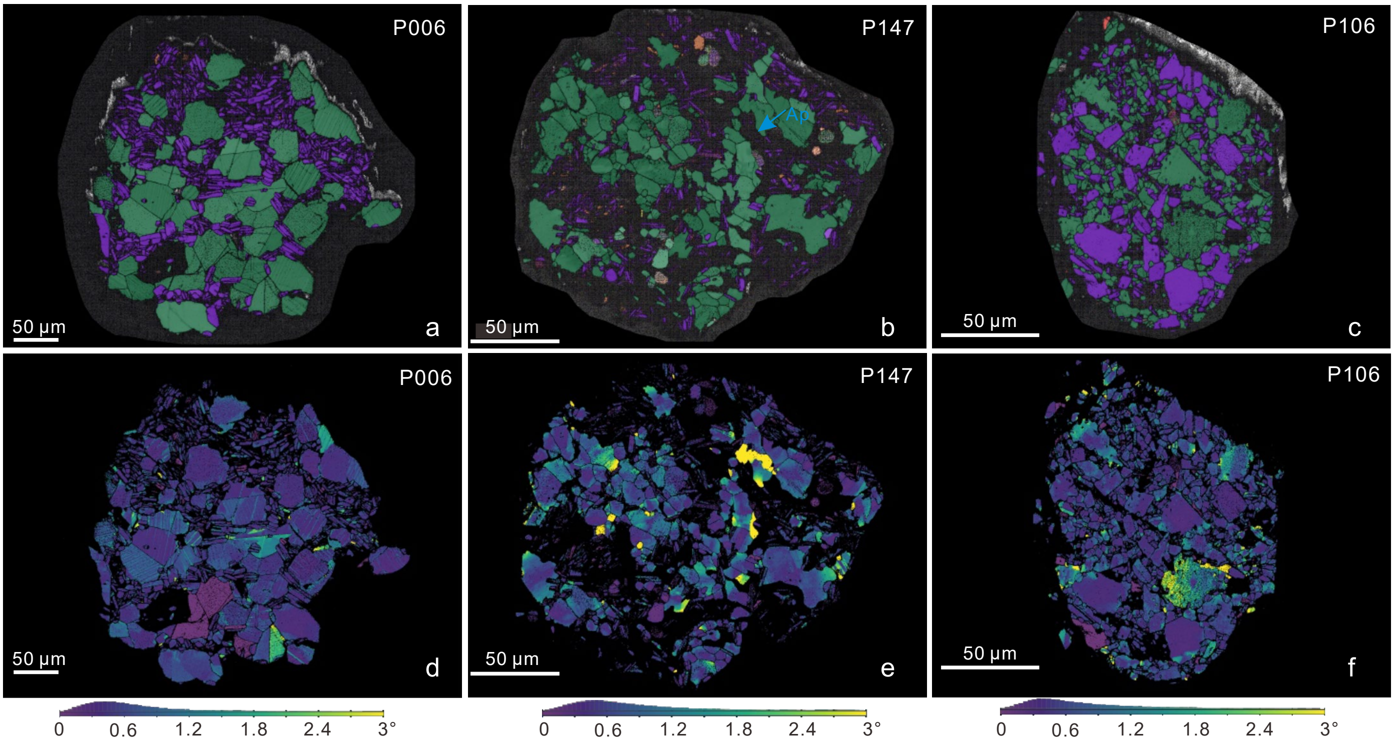

Extended Data Fig. 2 | EBSD maps of three studied CE-6 lithic fragments. (**a-c**), phase mappings, different colors are identified as crystal, and black regions are glass within clasts; clinopyroxene (green), plagioclase (purple), K-feldspar (light orange). (**d-f**), disorientation mappings, light colors represent a high orientation and dark colors represent a low orientation. The color bar represents the crystal orientation distribution. Note that, some pigeonites in P106 and P147 have higher crystal orientations, as shown by their light color.

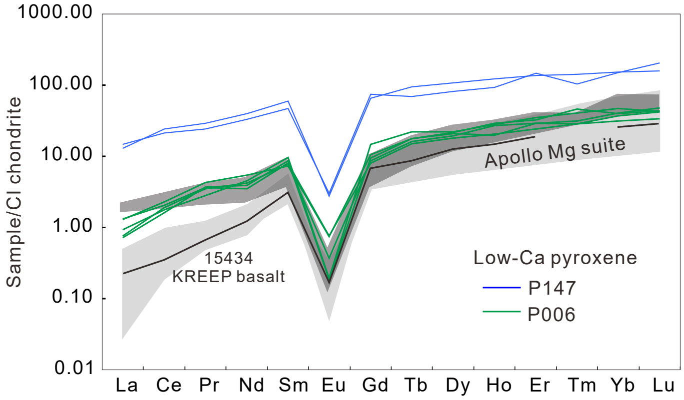

Extended Data Fig. 3 | REE patterns of the low-Ca pyroxene from CE-6 fragments. Low-Ca pyroxene from Apollo Mg-suite and QMD are shown for comparison. Data source: Mg-suite[69]; QMD[23]; Apollo 15434 KREEP basalt[25]; CI chondrite[70].

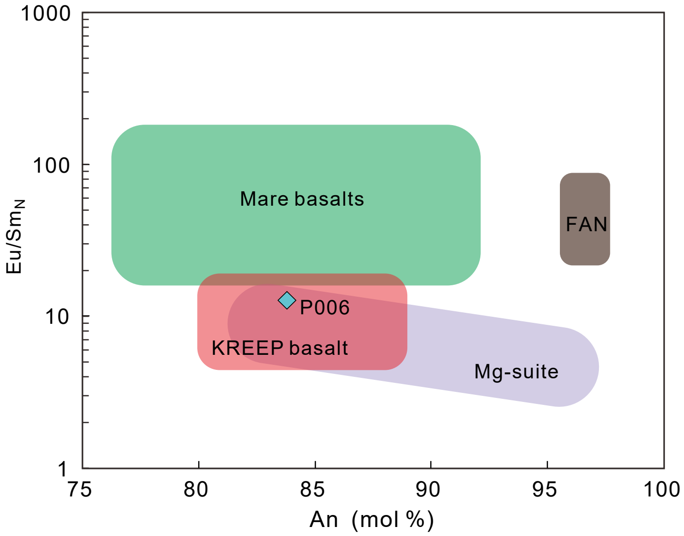

Extended Data Fig. 4 | CI chondrite-normalized Eu/Sm ratio versus An content of plagioclases in the P006 fragment. The compositional ranges of pristine lunar igneous rocks are from the compilation of[71].

https://doi.org/10.1038/s41550-025-02640-5

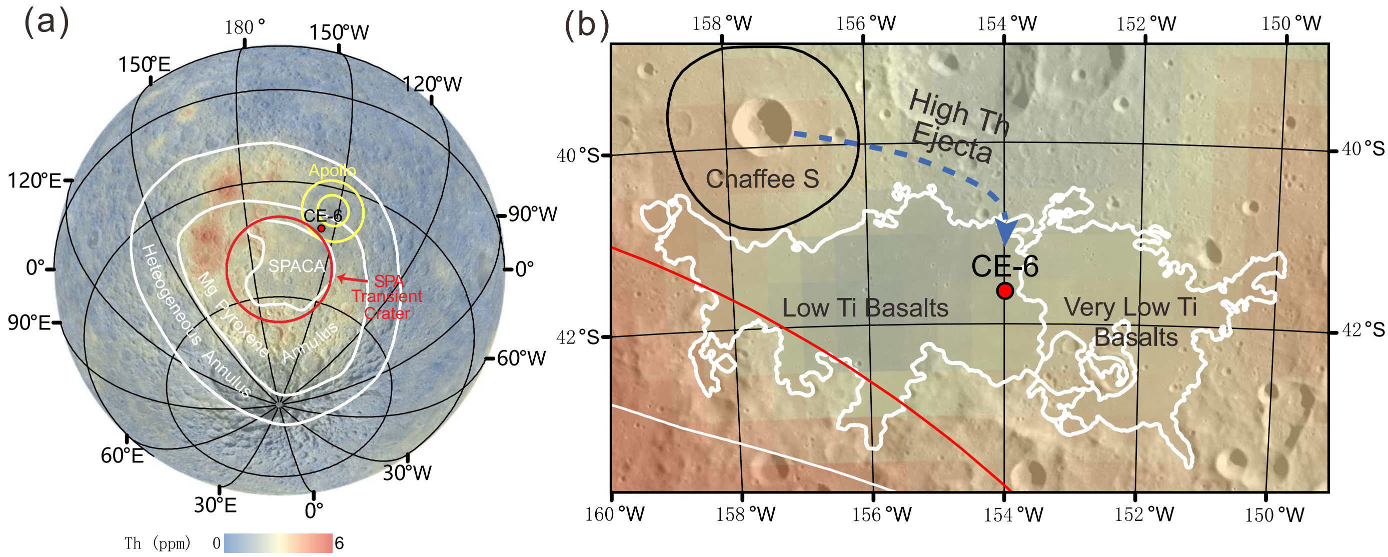

Extended Data Fig. 5 | Th abundance around the Chang'e-6 landing site. (**a**) The hemispheric thorium (Th) element mapping[29] shows the Th distribution relationships between the South-Pole Aitken (SPA) basin and Apollo basin where the CE-6 mission landed (Solid red dot); It is evident that the region around the SPA center (estimated transient crater; red circle) show elevated Th abundance, but the Apollo basin region shows lower Th abundance than its surroundings along the SPA topographic rim; Color bar represents the Th abundance. (**b**) The enlarged Th mapping shows the Th variations between the CE-6 sampling site and the nearby Chaffee S crater to the northwest. The Chaffee S crater region shows a slightly higher Th abundance than to its eastern. The Th-bearing ejecta material from the Chaffee S crater are highly likely to have been delivered into the CE-6 sampling site area. Red and white lines represent the boundary of SPA estimated transient crater[72] and SPA Compositional Anomaly (SPACA) region[6], respectively, which are marked in the image (**a**).

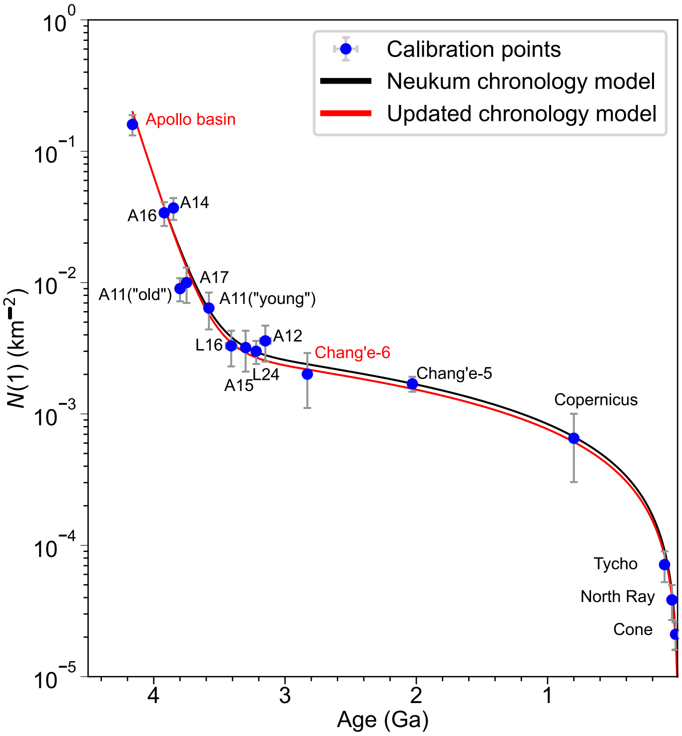

Extended Data Fig. 6 | An anchor point for the early lunar impact flux by the Apollo basin. The new calibration point of lunar impact flux based on the isotopic age of the Apollo basin and the representative crater density at the Apollo basin (red dot; see Methods). The classic crater chronology model[42] (black line) and a recently updated version using the calibration point established for the CE-5[60,73] and CE-6 mare basalts[20] (red line) are shown for comparisons. Calibration points (blue dots) are established from Apollo and Luna samples include crater densities[59,74], and radiometric ages[61]. The production densities use the N(1) value, which is the spatial density of craters with diameters of ≥1 km per square kilometer.

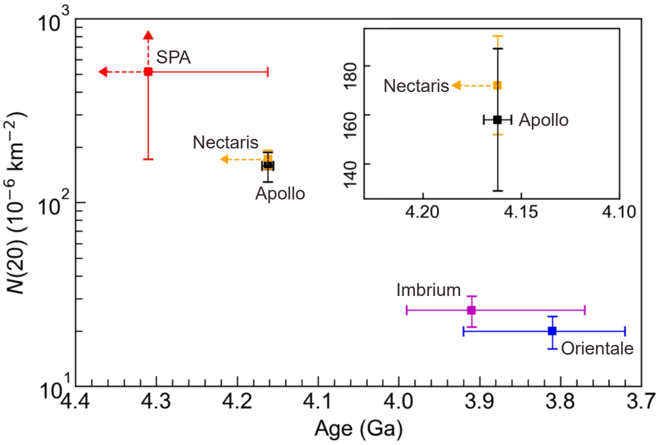

Extended Data Fig. 7 | Comparison of crater densities and age ranges of key impact basins on the Moon whose formation ages are related to the impact flux during LHB. Use of *N*(20) and age ranges are from[14,17]. The inset figure shows an enlarged comparison of the Nectaris and Apollo basins, and the Nectaris basin is older than 4.16 Ga.